

# GaAs Quantum Dot in a Parabolic Microcavity Tuned to $^{87}\text{Rb}$ $D_1$

Thomas Lettner,<sup>\*,†</sup> Katharina D. Zeuner,<sup>†</sup> Eya Schöll,<sup>†</sup> Huiying Huang,<sup>‡</sup> Selim Scharmer,<sup>†</sup> Saimon Filipe Covre da Silva,<sup>‡</sup> Samuel Gyger,<sup>†</sup> Lucas Schweickert,<sup>†</sup> Armando Rastelli,<sup>‡</sup> Klaus D. Jöns,<sup>\*,†</sup> and Val Zwiller<sup>†</sup>

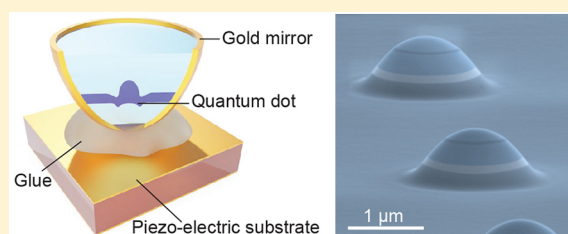
<sup>†</sup>Department of Applied Physics, Royal Institute of Technology, Albanova University Centre, Roslagstullsbacken 21, 106 91 Stockholm, Sweden

<sup>‡</sup>Institute of Semiconductor and Solid State Physics, Johannes Kepler University Linz, 4040 Linz, Austria

## Supporting Information

**ABSTRACT:** We develop a structure to efficiently extract photons emitted by a GaAs quantum dot tuned to rubidium. For this, we employ a broadband microcavity with a curved gold backside mirror that we fabricate by a combination of photoresist reflow, dry reactive ion etching in an inductively coupled plasma, and selective wet chemical etching. Precise reflow and etching control allows us to achieve a parabolic backside mirror with a short focal distance of 265 nm. The fabricated structures yield a predicted (measured) collection efficiency of 63% (12%), an improvement by more than 1 order of magnitude compared to unprocessed samples. We then integrate our quantum dot parabolic microcavities onto a piezoelectric substrate capable of inducing a large in-plane biaxial strain. With this approach, we tune the emission wavelength by 0.5 nm/kV, in a dynamic, reversible, and linear way, to the rubidium  $D_1$  line (795 nm).

**KEYWORDS:** semiconductor quantum dots, single-photon source, strain tuning, microcavity, two-photon resonance fluorescence, extraction efficiency



Quantum photonics is making significant progress due to the development of novel single-photon sources based on semiconductor quantum dots providing single and entangled photon generation on demand, with high purity, near-unity indistinguishability, and tunable emission energy.<sup>1,2</sup> They are therefore currently of high relevance in quantum information processing applications,<sup>3</sup> such as quantum networks, quantum simulation, and quantum cryptography. Strain-free gallium arsenide (GaAs) quantum dots obtained by etching and infilling nanoholes<sup>4,5</sup> offer record low multiphoton probability,<sup>6</sup> near-unity indistinguishability,<sup>7</sup> and near-unity entanglement fidelity<sup>8</sup> and have been used to demonstrate quantum teleportation,<sup>9</sup> as well as entanglement swapping.<sup>10,11</sup> In addition, they emit close to rubidium transitions, making them suitable for hybrid artificial and natural atomic systems.<sup>12</sup>

Currently, crucial remaining challenges for single and entangled photon sources based on the biexciton–exciton cascade lie in achieving (i) near-unity broadband extraction efficiency, (ii) efficient fiber coupling, and (iii) control over the spectral spread of the emitters. There exist several strategies to address each of these challenges independently, such as solid immersion lenses,<sup>13–15</sup> microlenses,<sup>16–18</sup> nanowires,<sup>19</sup> trumpets,<sup>20</sup> and circular Bragg resonators<sup>21–23</sup> to realize the desired extraction efficiency. Similarly, several approaches for efficient fiber coupling based on microstructures are available, such as metal-coated nanocones<sup>24</sup> and optical horn antennas.<sup>25</sup> Still, due to complex structure designs or nonplanar geometries,

integration with strain-tuning techniques remains challenging. In particular, piezoelectric actuators have emerged as a powerful method for tuning quantum dot properties,<sup>26</sup> where the induced strain allows to reversibly adjust the emission wavelength of quantum dots in microcavities<sup>27–30</sup> as well as their fine structure splitting.<sup>31–34</sup> However, the desired device combining broadband microcavities, Gaussian emission profile for fiber coupling, and tuning to generate on-demand wavelength-tunable single photons has not been realized so far.

Here, we demonstrate a device featuring GaAs quantum dots in parabolic gold back mirror microcavities integrated on a piezoelectric actuator (see Figure 1a), where the parabolic mirrors increase the extraction efficiency by redirecting the quantum dot emission toward the collection optics with a Gaussian farfield radiation pattern, while the piezoelectric actuator allows tuning of the quantum dot emission wavelength. In contrast to optical horn structures demonstrated for InAs/InP QDs,<sup>35</sup> the parabolic mirror has a much stronger focusing effect, which reduces the required cavity length by a factor 15, allowing for easier fabrication and strain-tunability. Furthermore, the parabolic microcavities operate over a broad wavelength range of several tens of nm. This is especially useful for enhancing both the exciton and biexciton emission lines simultaneously, crucial for entangled photon pair generation by the cascaded emission. The broadband nature of our

Received: August 28, 2019

Published: December 19, 2019

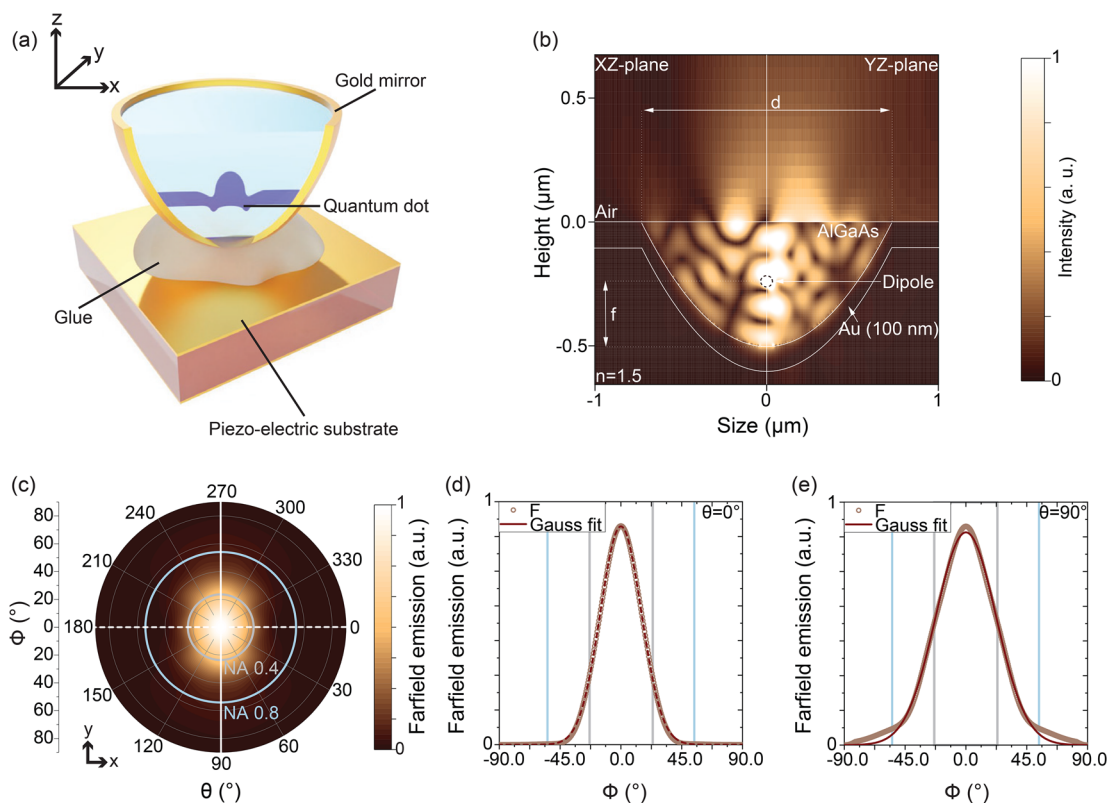


**Figure 1.** Strain-tunable quantum dot in parabolic mirror cavity. (a) The device concept features a quantum dot embedded in a parabolic microcavity mounted onto a piezoelectric substrate to strain-tune the emitter. (b–e) Finite-difference time-domain simulation results, with (b) vertical cuts in the  $xz$ - (left) and  $yz$ - (right) plane of the electric field distribution for a dipole with wavelength 795 nm in the focal point and oriented along  $x$ . The structure directs the emission toward the top along  $z$ . The diameter  $d$  is  $1.45\ \mu\text{m}$  and the height  $h$  is 500 nm, resulting in a focal length  $f$  of 265 nm. (c) Far-field emission profile for the top hemisphere. Two typical values for the numerical aperture (NA) of the collection lens are indicated (NA = 0.8, light blue and NA = 0.4 light gray). 90% radiates into an NA of 0.8 typical for high NA objectives. (d, e) Cut of the far-field emission along  $x$  and  $y$ , respectively, and fitted to a Gaussian distribution.

microcavity further enables multicolor excitation schemes<sup>36</sup> and complex multistage state initialization required for cluster state generation.<sup>37</sup>

We realize this structure with a novel fabrication method based on photoresist reflow<sup>38</sup> and dry etching. Our method offers high throughput, typically, we obtain more than 50 thousand paraboloids in one shot. Consequently, given a typical quantum dot density of below  $1/\mu\text{m}^2$ , hundreds of paraboloids contain a single quantum dot even without resorting to deterministic positioning. With this approach we observe up to 21.6 times increased brightness compared to the as-grown quantum dots, while simultaneously being able to strain-tune these bright emitters to the  $^{87}\text{Rb}$   $D_1$  transition.

The paraboloid's flat top surface allows for future fabrication of electrical contacts enabling the control of the charge state by applying an electric field through a diode structure with embedded quantum dots. Furthermore, typical diameters of the parabolic microcavities are comparable to the core diameter of standard optical fibers. The flat surface design allows for a direct integration of the fiber from top. To achieve high coupling efficiencies requires large mode overlap, which can be achieved by adjusting the diameter of our structures and precise emitter positioning.

## ■ DEVICE SIMULATION AND FABRICATION

To optimize the geometry and estimate the possible figures of merit, we simulate the structure with Lumerical using the

finite-difference time-domain method in 3D and extract the electromagnetic field distribution in the near and far field (Figure 1b). The quantum dot is simulated using a point dipole with an emission wavelength of 795 nm and embedded in a paraboloid with the refractive index of  $\text{Al}_{0.4}\text{Ga}_{0.6}\text{As}$ . The height ( $h$ ) of the paraboloid is set to 500 nm and the focal length ( $f$ ) is set to 265 nm to match the position of the quantum dot, which corresponds to a diameter ( $d$ ) of  $1.45\ \mu\text{m}$ . The curved sidewall of the paraboloid is surrounded by a gold mirror with a thickness of 100 nm. In Figure 1b, we plot the electric field distribution for vertical cuts in the  $xz$ - and  $yz$ -plane, respectively, where we observe a standing wave pattern inside the cavity formed by the parabolic mirror and the  $\text{Al}_{0.4}\text{Ga}_{0.6}\text{As}$ –air interface. Figure 1c shows the far-field emission profile of the top hemisphere, with numerical aperture (NA) of 0.8 (0.4) marked with light blue (gray) rings. The integrated intensity collectable with a typical objective (lens) with NA = 0.8 (NA = 0.4) is above 90% (50%). Figure 1d,e shows a cut of the emission profile along  $x$  (solid white line in Figure 1c) and  $y$  (dashed white line in Figure 1c), respectively, where the simulated far field intensity distribution (circles) closely follows a Gaussian distribution (solid line), one crucial requirement for efficient coupling into single mode fibers.

We study the influence of the structural dimensions of the paraboloid by sweeping the diameter while keeping the height fixed and monitoring the extraction efficiency together with the far field emission pattern. We also extract the Purcell factor,

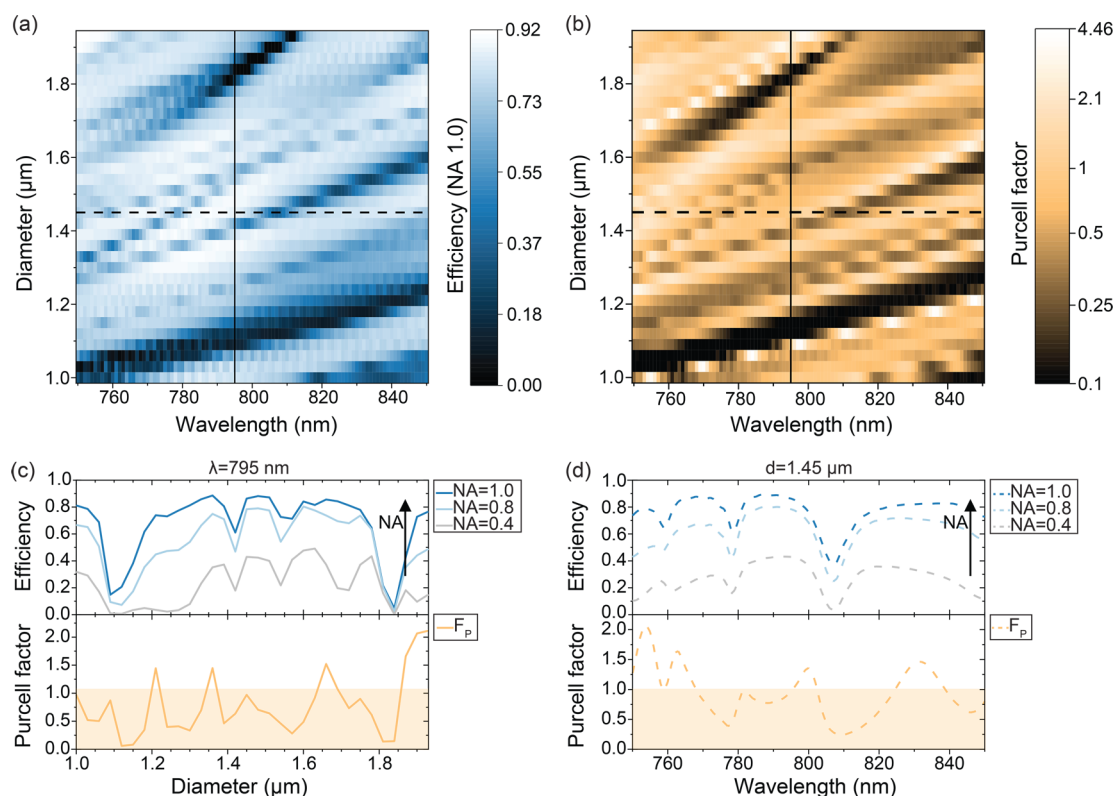


**Figure 2.** Simulation results for determining the ideal dimensions of the structure with (a) extraction efficiency and (b) Purcell factor as a function of diameter and source wavelength. The height of the structure (500 nm) and position of the quantum dot (265 nm from the bottom) are kept fixed. The solid and dashed lines represent cuts for a wavelength  $\lambda$  of 795 nm and a diameter  $d$  of 1.45  $\mu\text{m}$ , respectively, shown in panels (c) and (d). (c, d) Collection efficiency (top) for various numerical apertures (NAs) and Purcell factor (bottom) as a function of (c) structure diameter for a source wavelength  $\lambda$  of 795 nm and (d) wavelength for a structure diameter  $d$  of 1.45  $\mu\text{m}$ . The light yellow boxes mark Purcell factors smaller than 1.

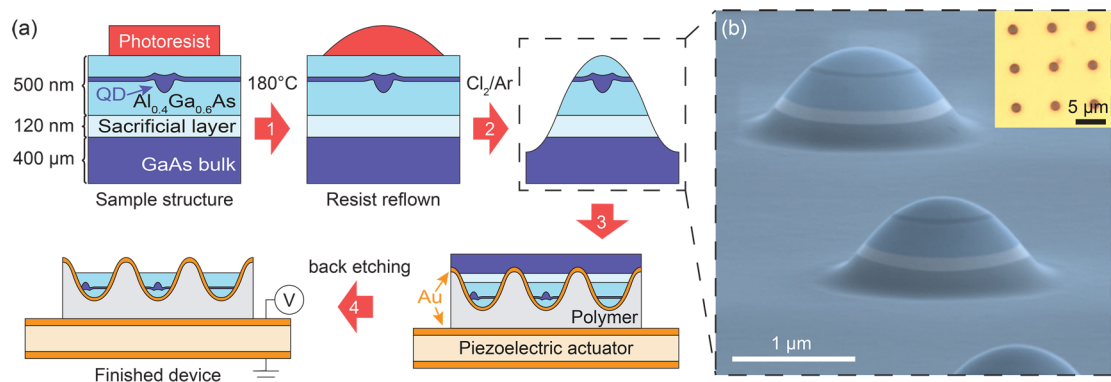


**Figure 3.** Fabrication of parabolic microcavity and integration onto the piezoelectric actuator. (a) Schematic of the quantum dot sample cross-section after photolithography. (1) Reflow of the photoresist into parabolic shape. (2) Dry-etching transfer of the photoresist profile. (3) Gold (Au) metallization and flip-chip integration onto the piezoelectric actuator. (4) Final selective wet chemical back etching and subsequent device contacting. (b) Colored scanning electron micrograph after step 2 of the sample surface under a viewing angle of 80°, where the layers with different aluminum-content are colored according to (a). Inset: Optical microscope image of the finished device.

which is defined as the power ratio emitted by the dipole inside the structure and that of the dipole in vacuum. Figure 2a,b shows the parameter sweep result of the extraction efficiency for an NA of 1.0 and the Purcell factor, respectively. We observe a complex pattern of bands and lines in both plots, with up to 92% extraction efficiency and Purcell factors reaching as high as 4.46 for certain parameter combinations. For  $d = 1.45 \mu\text{m}$  and 795 nm, which corresponds to the quantum dot sitting in the focal point of the paraboloid, the extraction efficiency is above 85% and the Purcell factor close

to 1. Moreover, the extraction efficiency for 795 nm stays close to 85% for a range of diameters from 1.2 to 1.8  $\mu\text{m}$  (vertical cut along the solid line in Figure 2c), thereby relaxing the fabrication requirements. At the same time, the extraction efficiency for  $d = 1.45 \mu\text{m}$  saturates close to 85% for a broad wavelength range from 780 to 800 nm (horizontal cut along the dashed line in Figure 2d). Finally, we also evaluate the collection efficiency for NA of 0.8 and 0.4 by integrating over the corresponding fraction of the far field (Figure 2c,d, light blue and gray lines).

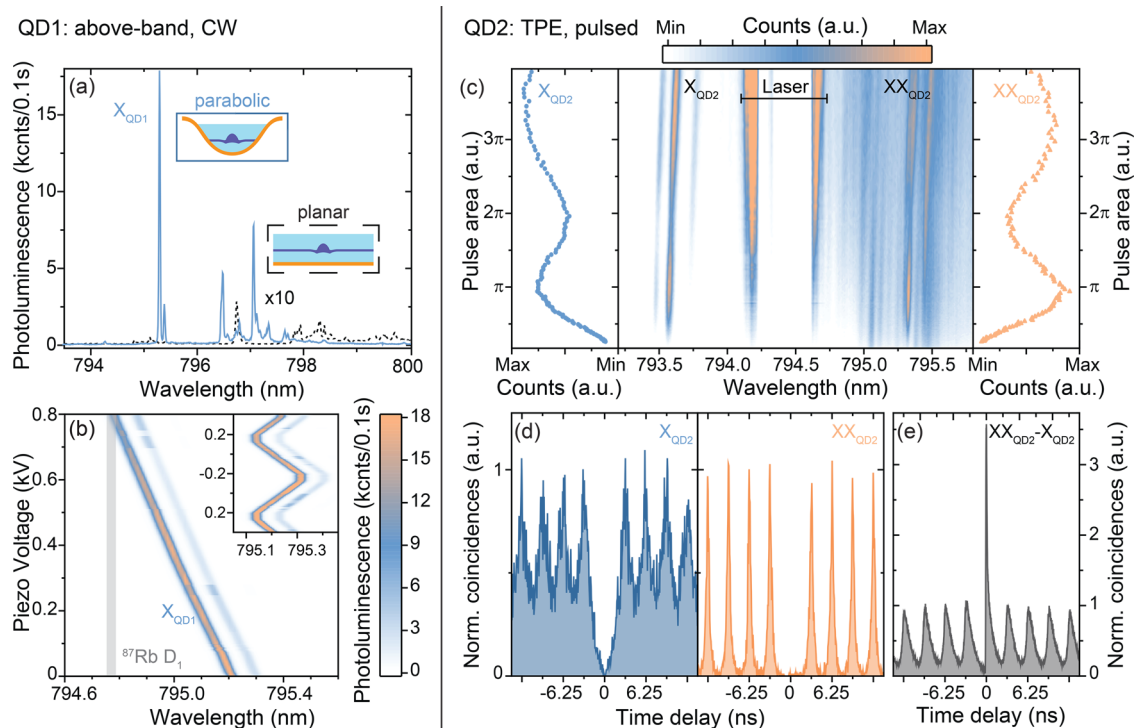


**Figure 4.** Microphotoluminescence characterization: (a, b) Spectrum of QD1 (blue, solid) in a parabolic microcavity under continuous wave above-band excitation with a green laser (a) compared to a 10 $\times$  magnified spectrum of a representative quantum dot in a planar structure (black, dashed) and (b) strain-tuning of the exciton ( $X_{\text{QD1}}$ ) of QD1 to the  $^{87}\text{Rb}$   $D_1$  (gray) transition by applying voltage to the piezoelectric actuator. (c–e) QD2 in a parabolic microcavity under pulsed two-photon resonant excitation (320 MHz repetition rate): (c) Color-coded microphotoluminescence spectra of QD2 as a function of the excitation pulse area showing Rabi oscillations for the exciton (left) and biexciton (right). (d) Second-order correlation measurement of the exciton ( $X_{\text{QD2}}$ ) and the biexciton ( $XX_{\text{QD2}}$ ) with  $g^{(2)}(0)$  of  $(0.013 \pm 0.004)$  for  $XX_{\text{QD2}}$  and (e) biexciton–exciton ( $XX_{\text{QD2}}-X_{\text{QD2}}$ ) cross-correlation measurement showing the cascaded emission.

The fabrication of the paraboloids by photoresist reflow, dry etching, subsequent flip-chip polymer gluing, and back etching is summarized in Figure 3a. We start with highly symmetric quantum dots of GaAs-infilled nanoholes obtained by aluminum droplet etching in  $\text{Al}_{0.4}\text{Ga}_{0.6}\text{As}$  grown by molecular beam epitaxy.<sup>39</sup> The distance of the quantum dot to the surface equals the target paraboloid focal length of 265 nm. A 120 nm thick layer of  $\text{Al}_{0.75}\text{Ga}_{0.25}\text{As}$  500 nm below the sample surface provides a sacrificial selective etch stop layer for the back etching step.

First, we spin-coat a 2  $\mu\text{m}$  thick layer of positive photoresist (S1818) before using maskless projection photolithography to define large arrays of photoresist circles with 2.1  $\mu\text{m}$  diameter separated by 7  $\mu\text{m}$ . On the same sample, we also design squares with 60  $\mu\text{m}$  side length (not shown in the schematic). The circles define the position of the parabolic back mirror structures and the squares conventional nanomembranes with flat back mirror serving as reference. Next, we reflow the photoresist, by placing the sample on a hot plate and increasing the temperature gradually to 180  $^\circ\text{C}$ , well above the glass transition temperature of the photoresist. We keep the temperature constant for 15 min in order to harden the photoresist for the dry etching. We then confirm by atomic force microscopy that this process reflows the photoresist circles into a paraboloid shape.

Then, we etch the sample by chemically assisted reactive ion etching with inductively coupled plasma of  $\text{Cl}_2$  and Ar for 2 min. The etching attacks both the exposed  $\text{Al}_{0.4}\text{Ga}_{0.6}\text{As}$  sample material and the photoresist covering the remaining sample surface. While they etch, the shape of the reflowed photoresist

paraboloids transfers into the  $\text{Al}_{0.4}\text{Ga}_{0.6}\text{As}$  underneath. The etching selectivity of  $\text{Al}_{0.4}\text{Ga}_{0.6}\text{As}$  over the photoresist depends on the etching parameters and modifies the aspect ratio of the obtained paraboloids. We utilize this for matching the focal length of the paraboloid with the distance of the apex to the quantum dot.

At this point we characterize the etched paraboloids, prior to metallization and piezoelectric actuator integration, by scanning electron microscopy. Figure 3b shows a colored scanning electron micrograph of paraboloids under a viewing angle of 80 $^\circ$ , where the coloring indicates the various layers in the semiconductor heterostructure which we observe due to the contrast from the difference in aluminum content of the layers. The etching step goes beyond the sacrificial layer and the resulting sidewalls appear smooth and rounded. From atomic force microscope measurements we obtain typically 5 nm for the root-mean-square roughness of the flat surface and deviations from the parabolic shape of 28 nm (see Supporting Information for more details).

In step 3 of the fabrication, we remove any residual photoresist by ashing in  $\text{O}_2$  plasma, deposit a bilayer of (Cr (5 nm)/Au (100 nm)) for the gold back mirror. Afterward, we flip and integrate the processed samples on the piezoelectric substrate with a polymer-based bonding process using SU-8. The substrate is 200  $\mu\text{m}$  thick and consists of single crystalline lead magnesium niobate-lead titanate (PMN–PT), which we lap, polish, and metallize with gold contacts prior to sample integration. Then we remove most of the bulk GaAs by nonselective chemical etching using  $\text{H}_3\text{PO}_4/\text{H}_2\text{O}_2 = 1:2$  and the remaining bulk GaAs with a selective etch consisting of

$C_6H_8O_7/H_2O_2 = 1:5$ . We remove the etch stop/sacrificial layer selectively with HCl, which we apply for 1 min at 30 °C. We are then able to observe the arrays of upside-down paraboloids sitting on top of the gold reflector, as defined by the photolithography design, under the microscope (inset in Figure 3b). Finally, we integrate the finished device on a custom aluminum nitride chip-carrier featuring gold contact pads using conductive silver glue and aluminum wire bonding.

## RESULTS AND DISCUSSION

For optical characterization we use confocal microphotoluminescence spectroscopy with our sample cooled to 5 K in a closed-cycle cryostat equipped with an NA 0.81 objective. We make sure to achieve proper poling of the piezoelectric actuator by biasing it with 150 V for the whole duration of the cooldown. Figure 4a shows the spectrally resolved photoluminescence of a quantum dot in a parabolic structure (QD1, solid blue line) in comparison to a quantum dot from the reference 60  $\mu\text{m}$  square nanomembrane with flat back mirror (dashed black line) from the same sample under above-band continuous-wave excitation with a green laser. The spectrum of the reference dot is representative for the quantum dots with flat mirror and has been magnified by a factor 10 for illustration purpose. Both spectra are very typical for Al droplet GaAs quantum dots, with an isolated exciton ( $X_{\text{QD1}}$ ) line at lower wavelength and an ensemble of lines at higher wavelengths. We further ensure that the excitation power is sufficient to saturate the emission from the X transition. The spectrum of QD1 shows an enhancement of more than 1 order of magnitude of all lines compared to the reference quantum dot. We calculate up to (on average) a 21.6 (6.2) times enhanced brightness for the parabolic microcavity quantum dots compared to the average integrated peak intensity of the as-grown quantum dots (see details in the Supporting Information). In comparison, the reference flat mirror quantum dots achieve on average only a factor of 1.6. We further extract from above-band pulsed excitation measurements a photon collection efficiency of 12% for the neutral exciton emission of a bright quantum dot in a parabolic microcavity, which is comparable to the values demonstrated for the optical horn structure.<sup>35</sup> This is still more than 6 times lower than our simulated value, which we attribute to the strong dependence of the efficiency on the lateral position of the quantum dot in the cavity and fabrication imperfections (see Supporting Information for more details).

In Figure 4b, we show photoluminescence spectra of the bright neutral exciton emission of QD1, which we tune to the atomic transition ( $^{87}\text{Rb } D_1$ ) of rubidium by applying a voltage of 800 V. As is typical for this piezoelectric tuning approach,<sup>26</sup> this tuning is linear and reversible. The emission lines of QD1 blue (red) shift by 0.5 nm by applying a positive (negative) voltage, respectively (see inset in Figure 4b). We observe no change in the emission after repeated voltage sweeps.

In Figure 4c–e, we show a parabolic microcavity quantum dot (QD2) under two-photon resonant excitation.<sup>40–42</sup> In this quantum dot, besides the separated exciton emission at low wavelength, we identify another line originating from the biexciton ( $XX_{\text{QD2}}$ ) appearing at higher wavelength around 795.3 nm.

To address the two-photon resonance of the biexciton, we excite QD2 with a wavelength-tunable pulsed laser with a repetition rate of 320 MHz and 6 ps pulse length, which we suppress with a cross-polarization setup and a tunable notch

filter. This excitation scheme drives the system coherently, as is evident in the excitation power-dependent resonance fluorescence measurements shown in Figure 4c. Both the biexciton (blue) and exciton (orange) lines show Rabi oscillations up to  $4\pi$  with the highest state occupation probability at a pulse area of  $\pi$ . We observe an increasing background which we attribute to phonon-assisted processes directly exciting the exciton state,<sup>43</sup> chirp in the laser excitation,<sup>42</sup> or unstabilized traps in the vicinity of the dot causing a population of the exciton state via fast discharging of other nonresonantly excited states. Furthermore, we observe a spectral red shift of the QD for higher excitation power, which we attribute to sample heating, stemming from light absorption in the metal layer and poor heat dissipation through the polymer layer.

For the time-correlated analysis, we filter the biexciton and exciton lines with a home-built transmission spectrometer (60% end-to-end efficiency, 19 GHz bandwidth) and detect the light with superconducting single photon detectors. We use a time correlator to generate time tagged files from the signals which we analyze with our Extensible Timetag Analyzer (ETA) software.<sup>44</sup> The second-order correlation measurements (Figure 4d) of the biexciton and exciton show a very low multiphoton probability indicated by the absence of the peak at zero time delay, with a  $g^{(2)}(0)$  of  $(0.013 \pm 0.004)$  for the biexciton, without background subtraction. For this, we sum up the coincidence events in equal time windows of 3.125 ns around each peak. We obtain the value for  $g^{(2)}(0)$  by calculating the ratio of the center peak at zero time delay and the average of four side peaks on each side. In the second-order correlation measurement of the exciton, the side peaks are overlapping due to the long lifetime of the state and the high repetition rate of our laser. The method described in the Supporting Information in ref 7 for the analysis of Hong-Ou-Mandel-type measurements can not be applied here, since the central peak is too small to extract individual time windows for the summation of coincidence events. Therefore, we do not give a value for the  $g^{(2)}(0)$  here; however, the measurement still shows a clear antibunching behavior for the exciton of QD2. In Figure 4e, we show the cross-correlation measurement between exciton and biexciton emission, recorded over 5 h and binned with 16 ps. We observe a strong and asymmetric peak due to the emission through the biexciton–exciton cascade leading to the detection of the biexciton before the exciton.

We conclude that, with our novel approach, by embedding GaAs quantum dots into parabolic gold mirror microcavities with broadband extraction efficiency enhancement, we realize high performance GaAs single photon emitters operating close to the  $^{87}\text{Rb } D_1$  transition. The fabrication method, based on photoresist reflow and a single dry etching step, allows for resilient fabrication of many devices per sample. Furthermore, we demonstrate straightforward integration on piezoelectric actuators to strain-tune the emission wavelength in a linear and reversible way to the  $^{87}\text{Rb } D_1$  line. The structures work under two-photon excitation with a fast 320 MHz repetition rate laser, providing clean single photons with a  $g^{(2)}(0)$  of  $(0.013 \pm 0.004)$  and at the same time pairs of photons from the biexciton–exciton cascade crucial for generation of polarization entangled photons. Of particular interest could be the potential use of the simulated Purcell factor to control the quantum dot emission lifetime. Further improvement could be achieved by (i) locating and precharacterizing specific quantum dots and fabricating parabolic mirror microcavities

around the emitters (see details in the [Supporting Information](#)), (ii) adding top gates for charge control, (iii) using micromachined piezoelectric actuators for increased strain tuning, and (iv) direct fiber coupling by lensed fiber gluing for easy and convenient plug-and-play operation.

## ■ ASSOCIATED CONTENT

### ● Supporting Information

The Supporting Information is available free of charge at <https://pubs.acs.org/doi/10.1021/acsp Photonics.9b01243>.

A GaAs quantum dot in a parabolic microcavity tuned to  $^{87}\text{Rb}$   $D_1$ : statistical evaluation and collection efficiency enhancement, simulation of a laterally displaced dipole, atomic force microscopy characterization of reflow photoresist and etched paraboloid, and simulations with atomic force microscopy data ([PDF](#))

## ■ AUTHOR INFORMATION

### Corresponding Authors

\*E-mail: [lettner@kth.se](mailto:lettner@kth.se).

\*E-mail: [klausj@kth.se](mailto:klausj@kth.se).

### ORCID

Thomas Lettner: 0000-0002-6434-2435

Huiying Huang: 0000-0002-8946-8472

Klaus D. Jöns: 0000-0002-5814-7510

### Notes

The authors declare no competing financial interest.

## ■ ACKNOWLEDGMENTS

This project has received funding from the Knut and Alice Wallenberg Foundation Grant “Quantum Sensors”, the Swedish Research Council (VR) through the VR Grant for International Recruitment of Leading Researchers (Ref 2013-7152), and from the European Union’s Horizon 2020 Research and Innovation Program (820423; S2QUIP). K.D.J. acknowledges funding from the Swedish Research Council (VR) via the starting Grant HyQRep (Ref 2018-04812) and the The Göran Gustafsson Foundation (SweTeQ). A.R. the Austrian Science Fund (FWF): P29603, the Linz Institute of Technology (LIT) and the LIT Secure and Correct Systems Lab supported by the State of Upper Austria. The Quantum Nano Photonics group at KTH acknowledges the continuous support by the companies APE Angewandte Physik und Elektronik GmbH on their picoEmerald system and Single Quantum BV on their SSPDs. We thank Martin Brunzell and Theodor Staffas for their help.

## ■ REFERENCES

- (1) Aharonovich, I.; Englund, D.; Toth, M. Solid-state single-photon emitters. *Nat. Photonics* **2016**, *10*, 631–641.
- (2) Senellart, P.; Solomon, G.; White, A. High-performance semiconductor quantum-dot single-photon sources. *Nat. Nanotechnol.* **2017**, *12*, 1026–1039.
- (3) Flamini, F.; Spagnolo, N.; Sciarrino, F. Photonic quantum information processing: a review. *Rep. Prog. Phys.* **2019**, *82*, No. 016001.
- (4) Heyn, C.; Stemann, A.; Köppen, T.; Strelow, C.; Kipp, T.; Grave, M.; Mendach, S.; Hansen, W. Highly uniform and strain-free GaAs quantum dots fabricated by filling of self-assembled nanoholes. *Appl. Phys. Lett.* **2009**, *94*, 183113.

(5) Gurioli, M.; Wang, Z.; Rastelli, A.; Kuroda, T.; Sanguinetti, S. Droplet epitaxy of semiconductor nanostructures for quantum photonic devices. *Nat. Mater.* **2019**, *18*, 799–810.

(6) Schweickert, L.; Jöns, K. D.; Zeuner, K. D.; Covre da Silva, S. F.; Huang, H.; Lettner, T.; Reindl, M.; Zichi, J.; Trotta, R.; Rastelli, A.; Zwiller, V. On-demand generation of background-free single photons from a solid-state source. *Appl. Phys. Lett.* **2018**, *112*, No. 093106.

(7) Schöll, E.; Hanschke, L.; Schweickert, L.; Zeuner, K. D.; Reindl, M.; Covre da Silva, S. F.; Lettner, T.; Trotta, R.; Finley, J. J.; Müller, K.; Rastelli, A.; Zwiller, V.; Jöns, K. D. Resonance Fluorescence of GaAs Quantum Dots with Near-Unity Photon Indistinguishability. *Nano Lett.* **2019**, *19*, 2404–2410.

(8) Huber, D.; Reindl, M.; Huo, Y.; Huang, H.; Wildmann, J. S.; Schmidt, O. G.; Rastelli, A.; Trotta, R. Highly indistinguishable and strongly entangled photons from symmetric GaAs quantum dots. *Nat. Commun.* **2017**, *8*, 15506.

(9) Reindl, M.; Huber, D.; Schimpf, C.; da Silva, S. F. C.; Rota, M. B.; Huang, H.; Zwiller, V.; Jöns, K. D.; Rastelli, A.; Trotta, R. All-photonic quantum teleportation using on-demand solid-state quantum emitters. *Science Advances* **2018**, *4*, eaau1255.

(10) Zopf, M.; Keil, R.; Chen, Y.; Yang, J.; Chen, D.; Ding, F.; Schmidt, O. G. Entanglement Swapping with Semiconductor-Generated Photons Violates Bell’s Inequality. *Phys. Rev. Lett.* **2019**, *123*, 160502.

(11) Basso Basset, F.; Rota, M. B.; Schimpf, C.; Tedeschi, D.; Zeuner, K. D.; da Silva, S. F. C.; Reindl, M.; Zwiller, V.; Jöns, K. D.; Rastelli, A.; Trotta, R. Entanglement swapping with photons generated on-demand by a quantum dot. *Phys. Rev. Lett.* **2019**, *123*, 160501.

(12) Akopian, N.; Wang, L.; Rastelli, A.; Schmidt, O. G.; Zwiller, V. Hybrid semiconductoratomic interface: slowing down single photons from a quantum dot. *Nat. Photonics* **2011**, *5*, 230–233.

(13) Zwiller, V.; Björk, G. Improved light extraction from emitters in high refractive index materials using solid immersion lenses. *J. Appl. Phys.* **2002**, *92*, 660–665.

(14) Sartison, M.; Portalupi, S. L.; Gissibl, T.; Jetter, M.; Giessen, H.; Michler, P. Combining in-situ lithography with 3D printed solid immersion lenses for single quantum dot spectroscopy. *Sci. Rep.* **2017**, *7*, 39916.

(15) Chen, Y.; Zopf, M.; Keil, R.; Ding, F.; Schmidt, O. G. Highly-efficient extraction of entangled photons from quantum dots using a broadband optical antenna. *Nat. Commun.* **2018**, *9*, 2994.

(16) Ma, Y.; Ballesteros, G.; Zajac, J. M.; Sun, J.; Gerardot, B. D. Highly directional emission from a quantum emitter embedded in a hemispherical cavity. *Opt. Lett.* **2015**, *40*, 2373–2376.

(17) Gschrey, M.; Thoma, A.; Schnauber, P.; Seifried, M.; Schmidt, R.; Wohlfeil, B.; Krüger, L.; Schulze, J.-H.; Heindel, T.; Burger, S.; Schmidt, F.; Strittmatter, A.; Rodt, S.; Reitzenstein, S. Highly indistinguishable photons from deterministic quantumdot microlenses utilizing three-dimensional in situ electron-beam lithography. *Nat. Commun.* **2015**, *6*, 7662.

(18) Sartison, M.; Engel, L.; Kolatschek, S.; Olbrich, F.; Nawrath, C.; Hepp, S.; Jetter, M.; Michler, P.; Portalupi, S. L. Deterministic integration and optical characterization of telecom O-band quantum dots embedded into wet-chemically etched Gaussian-shaped microlenses. *Appl. Phys. Lett.* **2018**, *113*, No. 032103.

(19) Claudon, J.; Bleuse, J.; Malik, N. S.; Bazin, M.; Jaffrennou, P.; Gregersen, N.; Sauvan, C.; Lalanne, P.; Gérard, J.-M. A highly efficient single-photon source based on a quantum dot in a photonic nanowire. *Nat. Photonics* **2010**, *4*, 174–177.

(20) Munsch, M.; Malik, N. S.; Dupuy, E.; Delga, A.; Bleuse, J.; Gérard, J.-M.; Claudon, J.; Gregersen, N.; Mørk, J. Dielectric GaAs Antenna Ensuring an Efficient Broadband Coupling between an InAs Quantum Dot and a Gaussian Optical Beam. *Phys. Rev. Lett.* **2013**, *110*, 177402.

(21) Davanço, M.; Rakher, M. T.; Schuh, D.; Badolato, A.; Srinivasan, K. A circular dielectric grating for vertical extraction of single quantum dot emission. *Appl. Phys. Lett.* **2011**, *99*, No. 041102.

- (22) Liu, J.; Su, R.; Wei, Y.; Yao, B.; Silva, S. F. C. d.; Yu, Y.; Iles-Smith, J.; Srinivasan, K.; Rastelli, A.; Li, J.; Wang, X. A solid-state source of strongly entangled photon pairs with high brightness and indistinguishability. *Nat. Nanotechnol.* **2019**, *14*, 586.
- (23) Wang, H.; et al. On-Demand Semiconductor Source of Entangled Photons Which Simultaneously Has High Fidelity, Efficiency, and Indistinguishability. *Phys. Rev. Lett.* **2019**, *122*, 113602.
- (24) Suemune, I.; Nakajima, H.; Liu, X.; Odashima, S.; Asano, T.; Iijima, H.; Huh, J.-H.; Idutsu, Y.; Sasakura, H.; Kumano, H. Metal-coated semiconductor nanostructures and simulation of photon extraction and coupling to optical fibers for a solid-state singlephoton source. *Nanotechnology* **2013**, *24*, 455205.
- (25) Grosjean, T.; Mivelle, M.; Burr, G. W.; Baida, F. I. Optical horn antennas for efficiently transferring photons from a quantum emitter to a single-mode optical fiber. *Opt. Express* **2013**, *21*, 1762–1772.
- (26) Martín-Sánchez, J.; et al. Strain-tuning of the optical properties of semiconductor nanomaterials by integration onto piezoelectric actuators. *Semicond. Sci. Technol.* **2018**, *33*, No. 013001.
- (27) Zander, T.; Herklotz, A.; Kiravittaya, S.; Benyoucef, M.; Ding, F.; Atkinson, P.; Kumar, S.; Plumhof, J. D.; Dörr, K.; Rastelli, A.; Schmidt, O. G. Epitaxial quantum dots in stretchable optical microcavities. *Opt. Express* **2009**, *17*, 22452–22461.
- (28) Lin, H.; Lin, C.-H.; Lai, W.-C.; Lee, Y.-S.; Lin, S.-D.; Chang, W.-H. Stress tuning of strong and weak couplings between quantum dots and cavity modes in microdisk microcavities. *Phys. Rev. B: Condens. Matter Mater. Phys.* **2011**, *84*, 201301.
- (29) Sun, S.; Kim, H.; Solomon, G. S.; Waks, E. Strain tuning of a quantum dot strongly coupled to a photonic crystal cavity. *Appl. Phys. Lett.* **2013**, *103*, 151102.
- (30) Moczala-Dusanowska, M.; Dusanowski, Ł.; Gerhardt, S.; He, Y. M.; Reindl, M.; Rastelli, A.; Trotta, R.; Gregersen, N.; Höfling, S.; Schneider, C. Strain-Tunable SinglePhoton Source Based on a Quantum Dot–Micropillar System. *ACS Photonics* **2019**, *6*, 2025–2031.
- (31) Seidl, S.; Kroner, M.; Högele, A.; Karrai, K.; Warburton, R. J.; Badolato, A.; Petroff, P. M. Effect of uniaxial stress on excitons in a self-assembled quantum dot. *Appl. Phys. Lett.* **2006**, *88*, 203113.
- (32) Plumhof, J. D.; Krápek, V.; Ding, F.; Jöns, K. D.; Hafenbrak, R.; Klenovský, P.; Herklotz, A.; Dörr, K.; Michler, P.; Rastelli, A.; Schmidt, O. G. Strain-induced anticrossing of bright exciton levels in single self-assembled GaAs/Al<sub>x</sub>Ga<sub>1-x</sub>As and In<sub>x</sub>Ga<sub>1-x</sub>As/GaAs quantum dots. *Phys. Rev. B: Condens. Matter Mater. Phys.* **2011**, *83*, 121302.
- (33) Zhang, J.; Wildmann, J. S.; Ding, F.; Trotta, R.; Huo, Y.; Zallo, E.; Huber, D.; Rastelli, A.; Schmidt, O. G. High yield and ultrafast sources of electrically triggered entangled-photon pairs based on strain-tunable quantum dots. *Nat. Commun.* **2015**, *6*, 10067.
- (34) Trotta, R.; Martín-Sánchez, J.; Wildmann, J. S.; Piredda, G.; Reindl, M.; Schimpf, C.; Zallo, E.; Stroj, S.; Edlinger, J.; Rastelli, A. Wavelength-tunable sources of entangled photons interfaced with atomic vapours. *Nat. Commun.* **2016**, *7*, 10375.
- (35) Takemoto, K.; Takatsu, M.; Hirose, S.; Yokoyama, N.; Sakuma, Y.; Usuki, T.; Miyazawa, T.; Arakawa, Y. An optical horn structure for single-photon source using quantum dots at telecommunication wavelength. *J. Appl. Phys.* **2007**, *101*, No. 081720.
- (36) He, Y.-M.; Wang, H.; Wang, C.; Chen, M.-C.; Ding, X.; Qin, J.; Duan, Z.-C.; Chen, S.; Li, J.-P.; Liu, R.-Z.; Schneider, C.; Atatüre, M.; Höfling, S.; Lu, C.-Y.; Pan, J.-W. Coherently driving a single quantum two-level system with dichromatic laser pulses. *Nat. Phys.* **2019**, *15*, 941–946.
- (37) Schwartz, I.; Cogan, D.; Schmidgall, E. R.; Don, Y.; Gantz, L.; Kenneth, O.; Lindner, N. H.; Gershoni, D. Deterministic generation of a cluster state of entangled photons. *Science* **2016**, *354*, 434–437.
- (38) Nussbaum, P.; Völkel, R.; Herzig, H. P.; Eisner, M.; Haselbeck, S. Design, fabrication and testing of microlens arrays for sensors and microsystems. *Pure Appl. Opt.* **1997**, *6*, 617–636.
- (39) Huo, Y. H.; Rastelli, A.; Schmidt, O. G. Ultra-small excitonic fine structure splitting in highly symmetric quantum dots on GaAs (001) substrate. *Appl. Phys. Lett.* **2013**, *102*, 152105.
- (40) Stufler, S.; Machnikowski, P.; Ester, P.; Bichler, M.; Axt, V. M.; Kuhn, T.; Zrenner, A. Two-photon Rabi oscillations in a single In<sub>x</sub>Ga<sub>1-x</sub>As/GaAs quantum dot. *Phys. Rev. B: Condens. Matter Mater. Phys.* **2006**, *73*, 125304.
- (41) Jayakumar, H.; Predojević, A.; Huber, T.; Kauten, T.; Solomon, G. S.; Weihs, G. Deterministic Photon Pairs and Coherent Optical Control of a Single Quantum Dot. *Phys. Rev. Lett.* **2013**, *110*, 135505.
- (42) Müller, M.; Bounouar, S.; Jöns, K. D.; Glässl, M.; Michler, P. On-demand generation of indistinguishable polarization-entangled photon pairs. *Nat. Photonics* **2014**, *8*, 224–228.
- (43) Reindl, M.; Jöns, K. D.; Huber, D.; Schimpf, C.; Huo, Y.; Zwiller, V.; Rastelli, A.; Trotta, R. Phonon-Assisted Two-Photon Interference from Remote Quantum Emitters. *Nano Lett.* **2017**, *17*, 4090–4095.
- (44) Lin, Z.; Schweickert, L. Timetag/eta: ETA 0.6.5. Zenodo 2019.